

VAE-CE: Visual Contrastive Explanation using Disentangled VAEs

Yoeri Poels Vlado Menkovski

Eindhoven University of Technology, the Netherlands

{y.r.j.poels, v.menkovski}@tue.nl

Abstract

The goal of a classification model is to assign the correct labels to data. In most cases, this data is not fully described by the given set of labels. Often a rich set of meaningful concepts exist in the domain that can much more precisely describe each datapoint. Such concepts can also be highly useful for interpreting the model’s classifications. In this paper we propose a model, denoted as Variational Autoencoder-based Contrastive Explanation (VAE-CE), that represents data with high-level concepts and uses this representation for both classification and generating explanations. The explanations are produced in a contrastive manner, conveying why a datapoint is assigned to one class rather than an alternative class. An explanation is specified as a set of transformations of the input datapoint, with each step depicting a concept changing towards the contrastive class. We build the model using a disentangled VAE, extended with a new supervised method for disentangling individual dimensions. An analysis on synthetic data and MNIST shows that the approaches to both disentanglement and explanation provide benefits over other methods¹.

1. Introduction

Discriminative models for classification based on deep neural networks achieve outstanding performance given a sufficient amount of training data. They are highly practical as they can be trained in an end-to-end fashion to develop a map $f : X \rightarrow Y$ given pairs of datapoints and labels (x, y) , with $x \in X$ and $y \in Y$. Much of this success is due to their hierarchical nature, which allows them to learn an effective high-level representation of low-level input data. However, these characteristics are also the reason for one of their major limitations. Even though the models learn high-level representations, in most cases the model’s reasoning is difficult to interpret. The learned representations are often hard to align with existing concepts in the domain. So, these models are commonly considered black boxes that directly

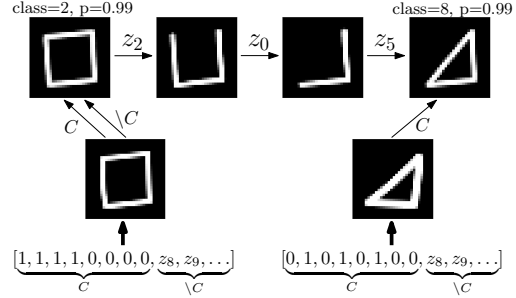


Figure 1: An example of an explanation where lines are concepts, and combinations thereof define classes. The query (left) and exemplar (right) datapoint differ in some class-relevant concepts in C . This difference is conveyed by transforming in domain C , one concept at a time.

map observations to target variables. Such black-box models often lack user trust[22, 32], as we cannot accurately gauge why they make the predictions they do.

Many interpretability approaches have been proposed that focus on developing interpretations of models’ decisions and internal representations. When the data consists of natural images, some of these interpretations rely on the human visual system such that interpretations are visualizations of the model’s internal representations of the data (e.g. saliency maps[31, 45] or component visualizations[36, 41]). In general, such interpretability approaches are limited to certain types of data and to the qualitative interpretation by domain experts. In this paper, we propose an approach that includes interpretability as an integral part of the model.

Specifically, our model consists of maps $f_c : X \rightarrow C$ and $f_y : C \rightarrow Y$, where C indicates the domain of higher-level human-understandable *concepts*. The first map f_c develops an encoding of each datapoint into the domain C that we then use to explain the model’s decisions. The second map f_y implements the downstream task of assigning a class value to the datapoint.

The explanations that we produce are *contrastive*. Contrastive explanation follows the human tendency of explaining an event by (implicitly) comparing it to some alternative

¹Code is available at <https://github.com/yoeripoels/vce>

event that did not take place[27, 34]. In our case, they convey why a datapoint belongs to a given class in contrast to some other class, by highlighting the differences as a *sequence of transformations* of the datapoint.

For the empirical evaluation in this study we used image data. This allows us to present the explanations in a *visual* form; an example is depicted in Fig. 1. In general, the method could produce contrastive explanations by a sequence of transformations in any data space.

To create suitable explanations we need to be able to represent the data in an interpretable concept space and be able to generate interpretable transformations against a contrastive target. For these purposes we use a generative latent variable model, specifically a disentangled Variational Autoencoder (VAE)[25, 42]. We employ existing methods that disentangle class-relevant from irrelevant information[4, 19, 55], as only the former is of interest w.r.t. domain C . We expand this model further with a new method for representing individual concepts in individual dimensions, focused on generating high-quality transitions when changing a single dimension. To develop the contrastive explanation, we define a target datapoint that is associated with the target class, referred to as the exemplar[35]. We then infer a sequence of transformations in the concept domain C that interpolates between the query datapoint and the exemplar. The exemplar is selected such that it is representative of its class, and such that the sequence of transformations is of minimum length.

We denote our approach as Variational Autoencoder-based Contrastive Explanation (VAE-CE). To be able to validate VAE-CE, we define a method for quantitatively evaluating explanations, resting on access to the true generating process of the data. Using synthetic and real data we quantitatively and qualitatively compare our method to similar methods and evaluate the individual components of our method. The two main contributions of this paper can be summarized as follows:

- We propose a method for disentangling latent dimensions in a VAE. This method is guided by pairs of images indicating changes that should (not) correspond to a change in a single dimension. (§3.2)
- We propose a method for generating visual contrastive explanations of a datapoints’ class assignment. This method considers conditioning a VAE to represent class concepts in individual dimensions in a subpart of the latent space, and uses this space to generate interpolations depicting the class-relevant concepts. (§3)

2. Related work

Literature most relating to our work considers the topics of explanation in the context of image classification using neural networks, and disentanglement in VAEs.

Image-classification explanations come in many shapes. Saliency-based methods[31, 45, 54] explain classifications by highlighting the contribution of pixels w.r.t. the decision. This approach is extended to project contributions w.r.t. an alternative class, creating contrastive explanations[38, 40]. To evaluate the pixel contributions in a black-box manner, one can perturb images rather than inspect model components, *e.g.* for class detections[43] or for contrasting classes[8]. Models with an attention mechanism[10, 52] fundamentally possess the mechanic of inspecting input contributions, although attention likely only noisily predicts the input features’ importance[47].

One can generate examples showing changes necessary to flip a class decision, denoted as counterfactuals, to explain differences in classification decisions[51]. Another method for conveying such differences considers highlighting regions within the query image and an alternative image, showing which pieces must be swapped to flip the decision[14]. The use of deep generative models, such as Generative Adversarial Networks (GANs)[13] and VAEs[25, 42], has been proposed to explain classification boundaries using a high-level space. Such methods, *e.g.* [11, 21, 28, 37, 44, 48], involve different approaches to training a generative model and interpolating in its latent space to convey the boundary between different classification targets. Alternatively, one can create translations conveying these boundaries using datapoints[39].

To interpret decisions one can also work with high-level concepts, *e.g.* by evaluating learned components[36, 41] or by identifying associations between prespecified concepts and classification decisions[23]. Concepts can also be an integral part of a model, *e.g.* by first detecting concepts and using them to classify in an interpretable fashion[1, 56]. Other examples of self-explaining methods consider generating text descriptions that provide a (contrastive) reason for the classification[16] and matching image parts to other samples in order to assign a class[5].

Disentanglement in VAEs can be defined as the notion that single latent dimensions are sensitive to changes in single generative factors while being invariant to changes in others[2, 17, 29]. It is also often used in the context of separating information related to some factor (*e.g.* a class label or a specific grouping) from unrelated information[3, 4, 55].

Unsupervised approaches generally extend the *ELBO*’s regularization term with extra assumptions about the latent space, *e.g.* [6, 17, 24]. Sharing similarities with our approach to disentanglement (§3.2), [57] propose learning a disentangled representation using pairs differing in a single dimension, maximizing mutual information. Regarding unsupervised disentanglement, [29] raised the question whether we can expect well-disentangled representations, showing that strong inductive biases or supervision are a necessity for learning and validating such representations.

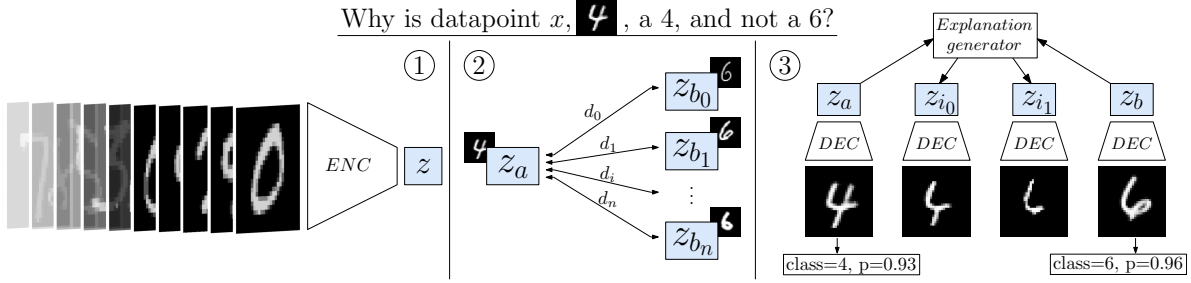


Figure 2: A simplified overview of the explanation generation method (we omit non-class factors for simplicity). (1) Encode a dataset to a semantically meaningful latent space. (2) In this space, find a suitable exemplar to contrast our query datapoint with. (3) Generate an interpolation highlighting the relevant concepts that distinguish the query from the exemplar.

Incorporating supervision, one approach is to group datapoints according to some shared feature and optimize a subpart of the latent space to share a representation for this group[3, 18, 20]. A weakly-supervised variant of this idea considers heuristically finding which dimensions are common and sharing those[30]. Alternatively, one can use labels to encourage a disentangled latent space, *e.g.* by optimizing subspaces to contain or exclude information about a label using auxiliary classification objectives[4, 9, 19, 55].

3. Method: VAE-CE

3.1. Learning a data representation for explanation

To represent the data in a higher-level space, we use a VAE[25, 42]. A VAE aims to approximate a dataset’s distribution under the assumption that its samples x are generated according to some latent variable z . In other words, the aim is to model $p(x, z) = p(x|z)p(z)$. This relation is approximated using an encoder $q_\phi(z|x)$ and decoder $p_\theta(x|z)$ distribution, parameterized by deep neural networks, and optimized using a lower bound on the true likelihood of the data, the *ELBO*. The reparametrization trick[25] is used to (back)propagate through the latent variables.

Using a VAE we can both infer latent variables z given data x , and generate modified samples \tilde{x} given some modification in z . It provides us with the tools to work in concept domain C , for both classification and explanation purposes. However, not all information in x , and consequently in z , is necessarily class related. To overcome this issue we build upon work aimed at disentangling class-relevant from irrelevant information in a VAEs latent representation.

The VAE’s *ELBO* objective is extended with classification terms, in line with works such as [4, 9, 19, 55]. Latent variable z is split into subspaces z_y and z_x , where the former aims to contain class-relevant information and the latter should contain the remaining information. We use a separate encoder for inferring each latent subspace; the z_y encoder, $q_{\phi_y}(z_y|x)$, serves as the concept encoder, f_c .

We introduce categorical distributions $q_{\psi_y}(y|z_y)$ and

$q_{\psi_x}(y|z_x)$, parameterized by neural networks and optimized using their log-likelihoods. We refer to these as the latent spaces’ classifiers. The former, $q_{\psi_y}(y|z_y)$, is also used to infer class predictions, serving as f_y .

For training, we simultaneously optimize the parameters of both classifiers and both encoders using categorical cross-entropy. However, z_x should contain little information about label y . To learn such a label-agnostic subspace we reverse the loss’ gradients for z_x ’s encoder, $q_{\phi_x}(z_x|x)$, through a Gradient Reversal Layer[12].

For each loss term, the subscript denotes the parameters it optimizes. The loss terms are as follows:

$$\mathcal{L}_{\theta, \phi_y, \phi_x, \psi_y}(x, y) = \beta_y KL(q_{\phi_y}(z_y|x)||p_\theta(z)) \quad (1)$$

$$+ \beta_x KL(q_{\phi_x}(z_x|x)||p_\theta(z)) \quad (2)$$

$$- \mathbb{E}_{q_{\phi_y}(z_y|x), q_{\phi_x}(z_x|x)}[\log p_\theta(x|z_y, z_x)] \quad (3)$$

$$- \alpha \mathbb{E}_{q_{\phi_y}(z_y|x)}[\log(q_{\psi_y}(y|z_y))] \quad (4)$$

$$+ \alpha \mathbb{E}_{q_{\phi_x}(z_x|x)}[\log(q_{\psi_x}(y|z_x))], \quad (5)$$

$$\mathcal{L}_{\psi_x}(x, y) = -\mathbb{E}_{q_{\phi_x}(z_x|x)}[\log(q_{\psi_x}(y|z_x))], \quad (6)$$

with hyperparameters β_y , β_x and α . We approximate all expectations with single-sample Monte Carlo estimation. Prior distribution $p_\theta(z)$ is set to a standard factorized Gaussian, $\mathcal{N}(0, I)$, which allows us to compute (1) and (2) analytically[25]. Distribution $p_\theta(x|z_y, z_x)$ is assumed to be a factorized Gaussian with fixed variance, allowing us to approximate (3) by taking the squared error between the input and its reconstruction. (4), (5) and (6) optimize the log-likelihood of the categorical distributions and are computed using categorical cross-entropy. Note that (5) is a negation of (6): Both are computed in a single pass. An overview of the model is depicted in Fig. 3.

3.2. Pair-based dimension conditioning

To produce explanations that convey differences in class concepts, we must manipulate concepts individually. To exercise such control, we aim to learn a representation where individual z_y -dimensions control individual concepts. We

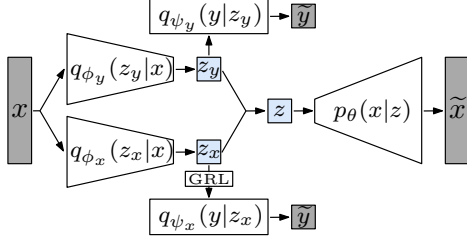


Figure 3: The architecture of the disentangled VAE. Datapoint x is encoded by two separate encoders into z_x and z_y , which are concatenated to reconstruct \tilde{x} . Disentanglement is encouraged by auxiliary classifiers. We omit the sampling procedure of the latent variables for clarity.

introduce a new disentanglement method based on two assumptions: (1) a significant change in a single latent dimension should correspond to changing a single concept and (2) we can train a model to evaluate whether changes fit this criterion. This method acts as additional regularization and is added on top of the previously described objective.

Two auxiliary models are used to aid the regularization procedure: A ‘Change Discriminator’ (CD) and a regular ‘Discriminator’ (D), both predicting a value in the range $[0, 1]$. CD is trained beforehand, and infers whether a pair of datapoints exhibits a desirable change. In our implementation, we train CD as a binary classifier with pairs that either indicate a good change (a single concept change) or a bad change (no or multiple concept changes); for details we refer to the supplementary material. D is trained to distinguish between generated and real datapoints, as done in a GAN[13].

By optimizing latent-dimension changes using CD as a critic, individual dimensions should better represent single concepts. D is used to optimize the quality of the samples to avoid a degenerate solution where non-realistic changes are produced that merely trick CD , rather than representing meaningful concept changes (*i.e.* an adversarial attack[49]).

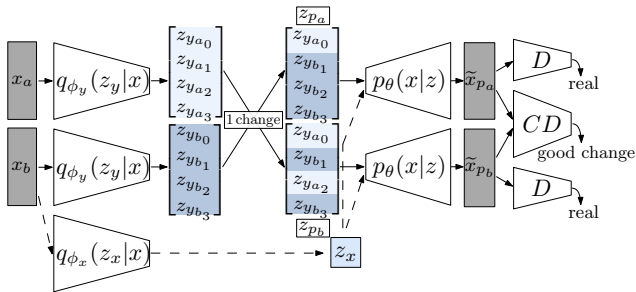


Figure 4: Individual dimensions are disentangled in an amortized fashion: Randomly constructed latent spaces differing in a single dimension are optimized to exhibit a desirable change in data space.

A visualization of the regularization procedure is depicted in Fig. 4. One step works as follows:

1. Encode two arbitrary (non-identical) datapoints x_a and x_b to their latent representations in z_y -space, giving us z_{y_a} and z_{y_b} . For the remaining information only encode the representation of datapoint x_b to z_x .
2. Construct two latent variables that share all but one dimension by combining z_{y_a} and z_{y_b} stochastically. We denote these variables as z_{p_a} and z_{p_b} . Each individual dimension comes from either z_{y_a} or z_{y_b} (equally likely), and all but one dimension are shared.
3. Map the constructed pair back to data space. That is, synthesize \tilde{x}_{p_a} and \tilde{x}_{p_b} by decoding latent representations (z_{p_a}, z_x) and (z_{p_b}, z_x) .
4. Optimize the encoders and the decoder such that CD predicts a high-quality change between \tilde{x}_{p_a} and \tilde{x}_{p_b} and D predicts that the samples are real.

The corresponding loss term is as follows:

$$\mathcal{L}_{\theta, \phi_y, \phi_x}(\tilde{x}_{p_a}, \tilde{x}_{p_b}) = -\alpha_r \log(D(\tilde{x}_{p_a})) \quad (7)$$

$$-\alpha_r \log(D(\tilde{x}_{p_b})) \quad (8)$$

$$+ \alpha_p n_y \frac{|z_{p_a} - z_{p_b}|}{|z_{y_a} - z_{y_b}|} \cdot -\log(CD(\tilde{x}_{p_a}, \tilde{x}_{p_b})), \quad (9)$$

with hyperparameters α_r and α_p , and n_y denoting the number of dimensions in z_y . This term optimizes the VAE such that CD and D predict high-quality changes and realistic datapoints. We scale the loss of CD 's prediction according to the difference in the dimension compared to the overall difference, multiplied by the number of dimensions. This extra scalar term ensures that we do not penalize ‘bad’ changes when the differing dimension is insignificant.

Discriminator D is trained in the same manner as a GAN’s discriminator, using \tilde{x}_{p_a} and \tilde{x}_{p_b} as fake data alongside real data from the training set; it learns to distinguish between them by minimizing the binary cross-entropy between the predicted labels and true/false labels.

3.3. Explanation generation

To explain a datapoint we focus on two aspects: Identifying a suitable exemplar and producing an explanation that displays the class concepts that differ between the datapoint and this exemplar. The exemplar is chosen from an alternative class, *e.g.* the second most likely class (given $q_{\psi_y}(y|z_y)$) or user selected. Alternatively, one could select a specific datapoint. An overview of the explanation procedure is provided in Fig. 2. When creating explanations we use mean values, rather than samples, of latent variable z . As such, we substitute z for μ in this subsection.

Exemplar identification rests on two principles: (1) how representative a datapoint is of its class and (2) how similar it is to the datapoint we contrast it with (as more similarity implies fewer concepts to change). To capture the former we only consider datapoints whose class probability is above a given threshold: $q_{\psi_y}(y_i|\mu_y) > t$. For the latter, we select the datapoint with the minimum squared difference in the class-specific subspace: $\min_b (\mu_{y_a} - \mu_{y_b})^2$, with a indicating the query datapoint and b the exemplar.

Explanation generation works by transforming the class-relevant latent embedding from the query (μ_{y_a}) to the exemplar (μ_{y_b}) and showcasing the intermediate steps; the class-irrelevant embedding (μ_{x_a}) is left unchanged. Dimension values are changed at once, as dimensions represent individual concepts. For each interpolation step, we allow multiple such dimension values to be switched, as there is no guarantee that every dimension difference depicts a concept changing (*i.e.* small differences are likely—but not necessarily—meaningless). We consider all orders of changing (groups of) dimensions; as dimensions can still be entangled, the interpolation path can have a significant effect on the quality of the intermediate states[7, 53].

The path we take to interpolate from μ_{y_a} to μ_{y_b} should be of minimum length, in line with the Minimum Description Length (MDL)[15] principle. Additionally, it is optimized w.r.t. two aspects: (1) each step should depict a single concept change and (2) each state should represent the dataset’s underlying distribution. These properties are optimized using auxiliary models CD and D .

Not all interpolation paths are explicitly computed, as the quantity of paths changing (groups of) dimensions grows extremely fast². Rather, we build a graph denoting all paths, where each edge denotes the cost of adding this state to the interpolation: A weighted sum of the probabilities of the change being undesirable (CD) and the datapoint being fake (D), adjusted by a normalization coefficient. For the change from μ_i to μ_j this can be computed as follows:

$$w_{ij} = [\alpha(1 - D(\tilde{x}_j)) + \beta(1 - CD(\tilde{x}_i, \tilde{x}_j))] \cdot k^\gamma, \quad (10)$$

where \tilde{x}_i and \tilde{x}_j are the reconstructed datapoints of states i and j , k is the number of dimensions changed, and α , β , and γ are hyperparameters. The shortest path in this graph represents the interpolation path optimized for our desiderata. An example of an interpolation graph is depicted in Fig. 5.

While the shortest path can be found in linear time w.r.t. the nodes and edges (since the graph is directed and acyclic[50]), the graph itself grows quickly. For n dimensions to change there are 2^n nodes and $3^n - 2^n$ edges (we refer to the supplementary material for a derivation). As such, this approach is only applicable to problems with a limited number of dimensions.

²Equivalent to the number of weak orderings of a set: Given n latent dimensions, the n^{th} Ordered Bell number[33].

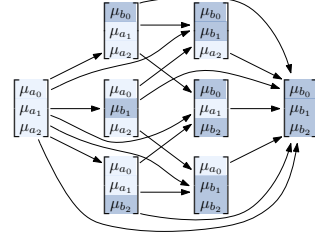


Figure 5: The interpolation graph of the transition between two latent variables of size 3 (weights omitted for clarity).

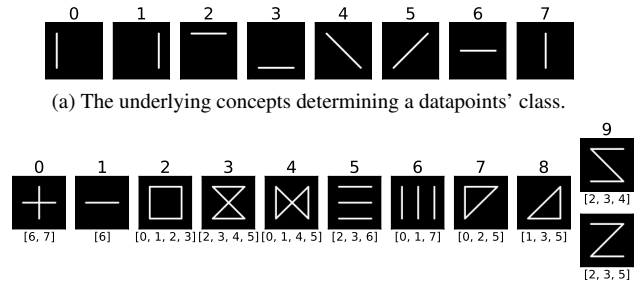
4. Experimental setup

4.1. Datasets

Synthetic data with a known generating process and set of concepts is used to validate our method in a controlled setting. The class determines the datapoints’ concepts, which together with added noise determine the datapoint. Concepts are defined as the occurrence of lines, where each line is defined by its orientation, length, and relative position. We use eight variables determining whether a specific line occurs in the data. The dataset consists of ten classes, with each class consisting of some combination(s) of lines. These lines and classes are depicted in Fig. 6.

Datapoints are generated by taking these ‘base shapes’ and adding non-trivial noise. The noise process seeks to mimic that of handwritten shapes (such as MNIST digits) and consists of shape distortion and line-width variation. We refer to the supplementary material for a detailed description of this generation procedure. Examples of synthetic datapoints are depicted in Fig. 7a.

The training and test set consist of 10 000 and 1000 32×32 -pixel images for each class, respectively. Model selection is done according to an explanation-quality metric that samples directly from the generative process (see §4.2), no validation set is used for tuning the model. Change pairs (for CD) are created by taking a class configuration and hiding some line(s) in both images in the pair, such that



(b) The ten classes in the dataset. The value above depicts the class index, whereas the value below depicts the indices of the lines that determine it.

Figure 6: An overview of the synthetic data’s structure.

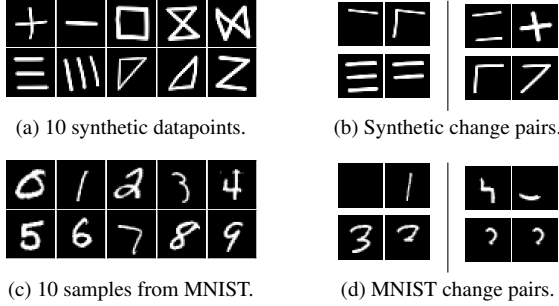


Figure 7: Synthetic data and MNIST, as used for training. Change pairs depicted on the left are positive (1 change), whereas those on the right are negative (0/2+ changes).

only 1 (positive) or 0/2+ lines differ (negative). Examples of such pairs are depicted in Fig 7b. Supervision used by other methods can be created using knowledge of the generative process. For each type of supervision we generate the same number of samples in total, 100 000.

MNIST[26] is used to evaluate our method in a more realistic setting, *i.e.* with noisy supervision. For ease of implementation, all images are padded to 32×32 pixels. No ground-truth concepts are available for MNIST. Consequently, we can only evaluate methods for which we can approximate the required supervision, and cannot evaluate metrics requiring ground-truth concept labels.

To create change pairs, images are augmented according to the notion that the concepts we reason with are continuous lines. Digits are reduced to individual lines and pixels are clustered according to these lines (we refer to the supplementary material for details). Using this line split, pairs are created that exhibit 1 (positive) or 0/2+ (negative) line changes. We create as many augmented pairs as there are training datapoints: 60 000. Examples of MNIST datapoints and change pairs are depicted in Figs. 7c and 7d. Creating a labeling of line types is a significantly more challenging task than augmenting individual images to create change pairs. As such, we do not consider methods requiring such supervision when evaluating MNIST.

4.2. Considered evaluations

Explanation alignment cost (*eac*). To the best of our knowledge there is no method for quantitatively evaluating explanations of our defined structure. As such, we introduce the explanation alignment cost (*eac*). The *eac* seeks to quantify the quality of a contrastive explanation based on a pair of datapoints a and b as input. The explanation consists of an interpolation starting at datapoint a , gradually transitioning to the *class-relevant* concepts of b (*i.e.* the final state of the transition is not necessarily identical to b). Each step should indicate a single concept being changed.

A candidate explanation for (a, b) is evaluated according

to the cost of aligning it to a ground-truth explanation. We define a ground-truth explanation as a minimum length sequence starting at a , with each subsequent state changing a single concept from a to b , with no other changes. The last state depicts a datapoint with all class-relevant concepts from b and the remaining information from a .

The alignments we identify must map every state in the candidate explanation to at least one state in the ground-truth explanation, and vice versa. Additionally, we constrain this mapping such that both aligned sequences are increasing. Such an alignment can be computed using Dynamic Time Warping (DTW)[46] in $O(nm)$ time (with n and m denoting the length of the explanations). We compute the cost of each individual state-to-state mapping as the per-pixel squared error and a constant, for discouraging (empty) repetitions in the alignment: $(x_c - x_t)^2 + \epsilon$, with x_c and x_t as states of the candidate and true explanation, and $\epsilon = .001$. We compute this cost for all possible ground-truth explanations ($n!$ orders, given n concepts to change) and take the minimum alignment cost as the *eac*. For evaluating the *eac* on the synthetic data, we compute the *eac* for 90 generated (a, b) pairs and report the average *eac*.

Representation quality metrics. Additionally, we explore the (adverse) effects of the conditioning methods on the learned representations. To quantify concept-disentanglement, the mutual information gap (*mig*)[6] is used. We estimate the *mig* for the class concepts in z_y following the same procedure as [29]. The *ELBO* metrics are also evaluated, denoted as *rec* (reconstruction error), kl_y , and kl_x (KL divergences of the subspaces). The classification accuracy, using the learned distribution $q_{\psi_y}(y|z_y)$, is denoted as *acc*. Finally, we evaluate the disentanglement of the latent subspaces w.r.t. class information, by training logistic regression classifiers on the latent space embeddings. Their accuracies are denoted as $l\text{-}acc_y$ and $l\text{-}acc_x$.

Other evaluations. We evaluate the exemplar identification by checking whether datapoints with more common concepts are more likely to be chosen. Class 9 has 2 variations, of which one variant has more concepts in common with classes 7 and 8. The remaining classes have the same number of concepts in common with both variants. We query for exemplars using 2000 test samples and compare the probability of selecting the more common variant using classes 7 and 8 to the probability when using other classes. Also, we qualitatively analyze the explanations, using both single datapoints to explain and input pairs to contrast.

4.3. Comparison overview

We compare VAE-CE to methods with similar capabilities, staying within the domain of VAE-based representation methods. The model described in §3.1 forms the baseline. We compare a set of alternative approaches to regularizing the z_y -space, alongside other interpolation approaches.

Concept-disentanglement methods. For each disentanglement approach we denote how we refer to it, alongside a short summarization of the regularization procedure and supervision. Some details differ from the original approaches as we adapt them to disentangle single dimensions and to be able to compare different types of supervision.

DVAE denotes the baseline model (§3.1). **LVAE** denotes an extension of label-based disentanglement as described in §3.1. For each z_y -dimension a label is provided indicating whether a concept is present. Each dimension is disentangled by two auxiliary classifiers, one predicting the label from the dimension value and one predicting the label from the remaining z_y dimensions. The latter objective’s gradients are reversed for the encoders. **GVAE** denotes an adaption of [18] using pairs of datapoints with (at least) one specified matching concept. The inferred values for the z_y -dimension corresponding to this concept are averaged out, forcing this information to be shared through optimizing the *ELBO*. **ADA-GVAE** denotes an adaption of [30] that uses positive change pairs as supervision, allowing us to compare to a method using similar supervision. Training is done using pairs of datapoints that differ in a single concept. We infer latent dimensions for both datapoints and average all but one dimension between the pair. The independent dimension is selected as the dimension with the highest KL divergence (between the pair). Optimization is again done using the *ELBO*. **VAE-CE** denotes our method (§3).

Model implementations. All methods share the same encoder and decoder architecture, and have a dimensionality of 8 for both z_x and z_y . Hyperparameters are optimized using the *eac* on a validation set of explanation pairs using synthetic data. As this cannot be evaluated for MNIST we use the same hyperparameters as chosen for the synthetic data; this approach resulted in reasonable models since the synthetic data was designed to share characteristics with MNIST. For details on architectures, training, and hyperparameters we refer to the supplementary material.

Interpolation methods. To evaluate the graph-based explanation approach, we also consider two naïve approaches to creating explanations. First, a smooth interpolation (denoted as *sm*), where each intermediate state of z_y is a convex combination of z_{y_a} and z_{y_b} . All dimensions are ad-

justed at once according to a predefined number of steps, in equal proportion for each step. We use five interpolation states. Second, a dimension-wise interpolation (denoted as *dim*), where we identify significantly differing dimensions with a simple heuristic: $|z_{y_{a_i}} - z_{y_{b_i}}| > 1$ (the σ of the prior). All significantly different dimensions are changed one at a time, in arbitrary order. The non-significant dimensions are changed at once, in the first step. Finally, for the graph-based interpolation (denoted as *graph*), we use explanation parameters $t = .95$ (exemplar threshold), $\alpha = .5$ (realism), $\beta = 1$ (change quality), and $\gamma = 1$ (normalization).

5. Results

All results are reported as mean \pm standard deviation, with the best mean marked in bold. We do more extensive comparisons using the synthetic data (both more methods and metrics) as access to ground-truth generative factors allows for more supervision and metric evaluations. For qualitative comparisons, other methods’ explanations are generated using the interpolation method with the lowest *eac* (*sm* or *dim*), whereas VAE-CE uses *graph*-based interpolation.

Synthetic data. For the *explanation quality*, the full results are provided in Table 2. VAE-CE provides the best results, the graph-based *eac* (i.e. the full method) is significantly lower than any other. As a small ablation study we also consider the *eac* given naïve interpolation methods, and use the graph-interpolation procedure and components from VAE-CE and apply it to other models. While the use of either component shows performance improvements, the scores are dominated by the combination thereof. Pair-based explanations and the closest ground-truths (as used for the *eac*) are depicted in Fig. 10. We can observe that VAE-CE transforms individual lines better than alternative approaches. Examples of individual explanations (from only a query datapoint) are depicted in Fig. 8a.

An overview of *representation-quality* metrics is provided in Table 1 (top). We can observe that the *mig* seems strongly correlated with the explanation quality, with VAE-CE performing best. Other metrics vary, with the baseline (DVAE) performing the best classification-wise. As such, the extra regularization comes at a cost.

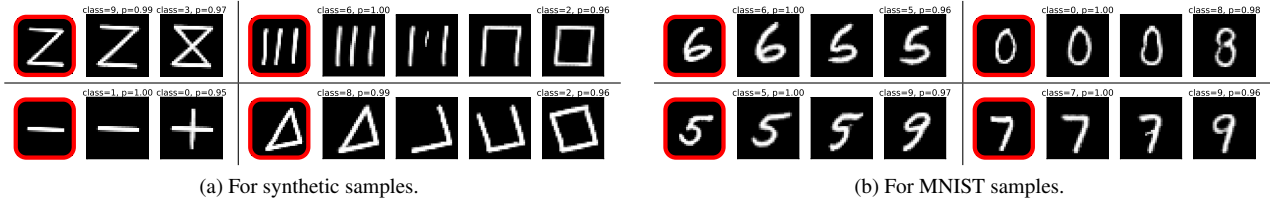


Figure 8: Explanations generated by VAE-CE. The query datapoints are outlined in red, followed by an explanation transforming the datapoint to the second most likely class.

Dataset	Model	$mig \uparrow$	$rec \downarrow$	$kl_y \downarrow$	$kl_x \downarrow$	$acc \uparrow$	$l-acc_y \uparrow$	$l-acc_x \downarrow$
Synthetic	DVAE	.1206 \pm .030	11.93 \pm .28	4.425 \pm .16	7.540 \pm .22	.9734 \pm .0007	.9749 \pm .0006	.1700 \pm .015
	LVAE	.4227 \pm .047	13.49 \pm 1.1	10.96 \pm 5.4	7.054 \pm .22	.9537 \pm .0080	.9618 \pm .0022	.2080 \pm .057
	GVAE	.1484 \pm .069	10.19 \pm .19	7.072 \pm .57	5.738 \pm .76	.9621 \pm .0010	.9641 \pm .0007	.2023 \pm .023
	ADA-GVAE	.3402 \pm .073	10.67 \pm .34	8.233 \pm 1.2	4.940 \pm 1.1	.9585 \pm .0008	.9610 \pm .0011	.1801 \pm .036
	VAE-CE	.4923 \pm .033	14.51 \pm .60	7.808 \pm .14	7.944 \pm .46	.9629 \pm .0009	.9657 \pm .0004	.1822 \pm .014
MNIST	DVAE		16.01 \pm .35	4.341 \pm .31	8.043 \pm .25	.9911 \pm .0007	.9940 \pm .0005	.1822 \pm .0094
	ADA-GVAE		13.64 \pm .19	10.14 \pm 1.1	3.604 \pm .90	.9645 \pm .0017	.9701 \pm .0015	.1997 \pm .015
	VAE-CE		21.67 \pm 1.34	7.117 \pm .29	6.646 \pm .35	.9795 \pm .0019	.9834 \pm .0017	.1817 \pm .012

Table 1: Representation quality metrics for synthetic data and MNIST.

Model	$eac-sm \downarrow$	$eac-dim \downarrow$	$eac-graph \downarrow$
DVAE	27.53 \pm .29	27.66 \pm .41	26.87 \pm .31
LVAE	26.95 \pm .45	25.38 \pm 1.6	23.86 \pm 1.0
GVAE	27.87 \pm .60	28.90 \pm .65	26.52 \pm .72
ADA-GVAE	26.84 \pm .57	26.22 \pm 1.1	23.24 \pm 1.2
VAE-CE	28.96 \pm .82	21.78 \pm .55	19.92 \pm .64

Table 2: Explanation quality results on the synthetic data. Note that *eac-graph* relies on VAE-CE components, other methods cannot independently produce these explanations.

For the *exemplar selection experiment*, the baseline probability of picking the evaluated variant of class 9 was $.7902 \pm .018$. Using classes 7 and 8 this variant was selected at a probability of $.9378 \pm .044$, hinting that a variant with more common factors is more likely to be chosen.

input	0 4	5 3
DVAE	0 0 4 4 4	5 5 5 3 3
ADA-GVAE	0 6 4 4	5 5 3 3 3 3
VAE-CE	0 0 4 4 4 4	5 3 3

Figure 9: MNIST explanations using provided input-pairs.

MNIST. The *explanation quality* is evaluated by comparing pair-based explanations and by evaluating datapoint-explanations. The resulting explanations are depicted in Figs. 9 and 8b, respectively. Although individual line changes are apparent in VAE-CE’s explanations they are noisier than before, likely because of the more complex shapes and noisy supervision. This is very apparent in e.g. the transition from 0-4 in Fig. 9. However, the other approaches do not explain well using the assumed concept of lines, but rather change multiple components at once.

The *representation quality* metrics are provided in Table 1 (bottom). These results paint a similar picture as before, with no method dominating all metrics. We note that DVAE’s accuracy is substantially higher than that of other methods, showing that the regularization methods again do not align perfectly with the representation of classes.

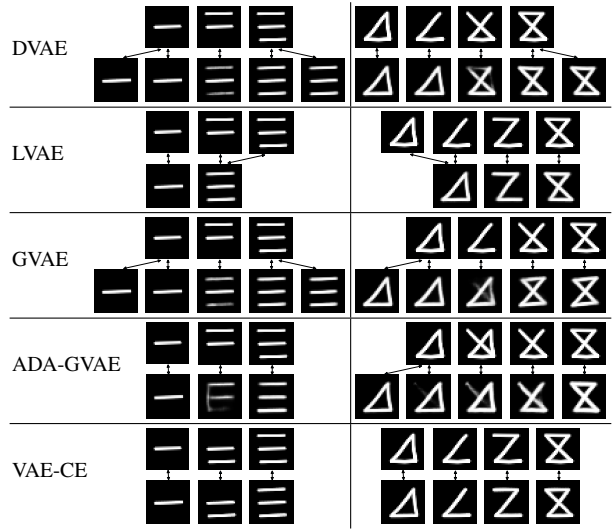


Figure 10: Synthetic-data explanations using provided pairs from class 1 to 5 (left) and class 8 to 3 (right). The top row indicates the closest ground-truth explanation, whereas the bottom row depicts the created interpolation.

6. Conclusions

In this paper, we proposed an interpretability-focused classification model that creates explanations in a concept domain \mathcal{C} . This method extends a class-disentangled VAE with a new supervised regularization method for disentangling individual dimensions. Using this model we generate visual contrastive explanations, highlighting class-differing concepts using a sequence of transformations. An introductory empirical evaluation shows that the components of our method provide benefits over existing approaches, although applying it to more complex data remains future work. Ultimately, we believe that the proposed method allows us to effectively learn a model that represents and explains data in domain \mathcal{C} , providing us with a more understandable and trustworthy classification model. Topics still of interest consider exploring more complex datasets, more efficient (heuristic search-based) approaches to explanation generation, and *CD* implementations using less supervision.

References

- [1] David Alvarez-Melis and Tommi S. Jaakkola. Towards robust interpretability with self-explaining neural networks. In *Proceedings of Advances in Neural Information Processing Systems 31*, pages 7786–7795, 2018.
- [2] Yoshua Bengio, Aaron Courville, and Pascal Vincent. Representation learning: A review and new perspectives. *IEEE transactions on pattern analysis and machine intelligence*, 35(8):1798–1828, 2013.
- [3] Diane Bouchacourt, Ryota Tomioka, and Sebastian Nowozin. Multi-level variational autoencoder: Learning disentangled representations from grouped observations. In *Proceedings of the Thirty-Second AAAI Conference on Artificial Intelligence*, pages 2095–2102, 2018.
- [4] Ruichu Cai, Zijian Li, Pengfei Wei, Jie Qiao, Kun Zhang, and Zhifeng Hao. Learning disentangled semantic representation for domain adaptation. In *Proceedings of the 28th International Joint Conference on Artificial Intelligence*, pages 2060–2066, 2019.
- [5] Chaofan Chen, Oscar Li, Daniel Tao, Alina Barnett, Cynthia Rudin, and Jonathan Su. This looks like that: Deep learning for interpretable image recognition. In *Proceedings of Advances in Neural Information Processing Systems 32*, pages 8928–8939, 2019.
- [6] Tian Qi Chen, Xuechen Li, Roger B. Grosse, and David Duvenaud. Isolating sources of disentanglement in variational autoencoders. In *Proceedings of Advances in Neural Information Processing Systems 31*, pages 2615–2625, 2018.
- [7] Ying-Cong Chen, Xiaogang Xu, Zhuotao Tian, and Jiaya Jia. Homomorphic latent space interpolation for unpaired image-to-image translation. In *Proceedings of the IEEE/CVF Conference on Computer Vision and Pattern Recognition*, pages 2408–2416, 2019.
- [8] Amit Dhurandhar, Pin-Yu Chen, Ronny Luss, Chun-Chen Tu, Pai-Shun Ting, Karthikeyan Shanmugam, and Payel Das. Explanations based on the missing: Towards contrastive explanations with pertinent negatives. In *Proceedings of Advances in Neural Information Processing Systems 31*, pages 590–601, 2018.
- [9] Zheng Ding, Yifan Xu, Weijian Xu, Gaurav Parmar, Yang Yang, Max Welling, and Zhuowen Tu. Guided variational autoencoder for disentanglement learning. In *Proceedings of the IEEE/CVF Conference on Computer Vision and Pattern Recognition*, pages 7917–7926, 2020.
- [10] Alexey Dosovitskiy, Lucas Beyer, Alexander Kolesnikov, Dirk Weissenborn, Xiaohua Zhai, Thomas Unterthiner, Mostafa Dehghani, Matthias Minderer, Georg Heigold, Sylvain Gelly, et al. An image is worth 16x16 words: Transformers for image recognition at scale. In *Proceedings of the 9th International Conference on Learning Representations*, 2020.
- [11] Amir Feghahati, Christian R. Shelton, Michael J. Pazzani, and Kevin Tang. CDeepEx: Contrastive deep explanations. In *Proceedings of the 24th European Conference on Artificial Intelligence*, pages 1143–1151, 2020.
- [12] Yaroslav Ganin and Victor S. Lempitsky. Unsupervised domain adaptation by backpropagation. In *Proceedings of the 32nd International Conference on Machine Learning*, pages 1180–1189, 2015.
- [13] Ian J. Goodfellow, Jean Pouget-Abadie, Mehdi Mirza, Bing Xu, David Warde-Farley, Sherjil Ozair, Aaron C. Courville, and Yoshua Bengio. Generative adversarial nets. In *Proceedings of Advances in Neural Information Processing Systems 27*, pages 2672–2680, 2014.
- [14] Yash Goyal, Ziyang Wu, Jan Ernst, Dhruv Batra, Devi Parikh, and Stefan Lee. Counterfactual visual explanations. In *Proceedings of the 36th International Conference on Machine Learning*, pages 2376–2384, 2019.
- [15] Peter D. Grünwald. *The minimum description length principle*. MIT press, 2007.
- [16] Lisa Anne Hendricks, Ronghang Hu, Trevor Darrell, and Zeynep Akata. Grounding visual explanations. In *Proceedings of the 15th European Conference on Computer Vision*, pages 269–286, 2018.
- [17] Irina Higgins, Loïc Matthey, Arka Pal, Christopher Burgess, Xavier Glorot, Matthew Botvinick, Shakir Mohamed, and Alexander Lerchner. beta-VAE: Learning basic visual concepts with a constrained variational framework. In *Proceedings of the 5th International Conference on Learning Representations*, 2017.
- [18] Haruo Hosoya. Group-based learning of disentangled representations with generalizability for novel contents. In Sarit Kraus, editor, *Proceedings of the 28th International Joint Conference on Artificial Intelligence*, pages 2506–2513, 2019.
- [19] Maximilian Ilse, Jakub M. Tomczak, Christos Louizos, and Max Welling. Diva: Domain invariant variational autoencoders. In *Proceedings of the International Conference on Medical Imaging with Deep Learning*, pages 322–348, 2020.
- [20] Ananya Harsh Jha, Saket Anand, Maneesh Singh, and V. S. R. Veeravasarapu. Disentangling factors of variation with cycle-consistent variational auto-encoders. In *Proceedings of the 15th European Conference on Computer Vision*, pages 829–845, 2018.
- [21] Shalmali Joshi, Oluwasanmi Koyejo, Warut Vijitbenjaronk, Been Kim, and Joydeep Ghosh. Towards realistic individual recourse and actionable explanations in black-box decision making systems. *arXiv preprint arXiv:1907.09615*, 2019.
- [22] Been Kim, Elena Glassman, Brittney Johnson, and Julie Shah. iBCM: Interactive bayesian case model empowering humans via intuitive interaction. 2015.
- [23] Been Kim, Martin Wattenberg, Justin Gilmer, Carrie J. Cai, James Wexler, Fernanda B. Viégas, and Rory Sayres. Interpretability beyond feature attribution: Quantitative testing with concept activation vectors (TCAV). In *Proceedings of the 35th International Conference on Machine Learning*, pages 2673–2682, 2018.
- [24] Hyunjik Kim and Andriy Mnih. Disentangling by factorising. In *Proceedings of the 35th International Conference on Machine Learning*, pages 2654–2663, 2018.
- [25] Diederik P. Kingma and Max Welling. Auto-encoding variational bayes. In *Proceedings of the 2nd International Conference on Learning Representations*, 2014.

- [26] Yann LeCun, Léon Bottou, Yoshua Bengio, and Patrick Haffner. Gradient-based learning applied to document recognition. *Proceedings of the IEEE*, 86(11):2278–2324, 1998.
- [27] Peter Lipton. Contrastive explanation. *Royal Institute of Philosophy Supplement*, 27:247–266, 1990.
- [28] Shusen Liu, Bhavya Kailkhura, Donald Loveland, and Yong Han. Generative counterfactual introspection for explainable deep learning. In *Proceedings of the 2019 IEEE Global Conference on Signal and Information Processing*, pages 1–5, 2019.
- [29] Francesco Locatello, Stefan Bauer, Mario Lucic, Gunnar Rätsch, Sylvain Gelly, Bernhard Schölkopf, and Olivier Bachem. Challenging common assumptions in the unsupervised learning of disentangled representations. In *Proceedings of the 36th International Conference on Machine Learning*, pages 4114–4124, 2019.
- [30] Francesco Locatello, Ben Poole, Gunnar Rätsch, Bernhard Schölkopf, Olivier Bachem, and Michael Tschannen. Weakly-supervised disentanglement without compromises. In *Proceedings of the 37th International Conference on Machine Learning*, pages 6348–6359, 2020.
- [31] Scott M. Lundberg and Su-In Lee. A unified approach to interpreting model predictions. In *Proceedings of Advances in Neural Information Processing Systems 30*, pages 4768–4777, 2017.
- [32] Joseph E. Mercado, Michael A. Rupp, Jessie Y. C. Chen, Michael J. Barnes, Daniel Barber, and Katelyn Procci. Intelligent agent transparency in human–agent teaming for Multi-UxV management. *Human factors*, 58(3):401–415, 2016.
- [33] István Mező. *Combinatorics and number theory of counting sequences*. Chapman and Hall/CRC, 2019.
- [34] Tim Miller. Explanation in artificial intelligence: Insights from the social sciences. *Artificial Intelligence*, 267:1–38, 2019.
- [35] Robert M. Nosofsky. Exemplar-based approach to relating categorization, identification, and recognition. *Multidimensional models of perception and cognition*, pages 363–393, 1992.
- [36] Chris Olah, Nick Cammarata, Ludwig Schubert, Gabriel Goh, Michael Petrov, and Shan Carter. Zoom in: An introduction to circuits. *Distill*, 2020.
- [37] Matthew R. O’Shaughnessy, Gregory Canal, Marissa Connor, Christopher Rozell, and Mark A. Davenport. Generative causal explanations of black-box classifiers. In *Proceedings of Advances in Neural Information Processing Systems 33*, 2020.
- [38] Michael J. Pazzani, Amir Feghahati, Christian R. Shelton, and Aaron R. Seitz. Explaining contrasting categories. In *Joint Proceedings of the ACM IUI 2018 Workshops co-located with the 23rd ACM Conference on Intelligent User Interfaces*, 2018.
- [39] Rafael Poyiadzi, Kacper Sokol, Raul Santos-Rodriguez, Tijl De Bie, and Peter Flach. FACE: Feasible and actionable counterfactual explanations. In *Proceedings of the AAAI/ACM Conference on AI, Ethics, and Society*, pages 344–350, 2020.
- [40] Mohit Prabhushankar, Gukyeon Kwon, Dogancan Temel, and Ghassan AlRegib. Contrastive explanations in neural networks. In *Proceedings of the IEEE International Conference on Image Processing*, pages 3289–3293, 2020.
- [41] Zhuwei Qin, Fuxun Yu, Chenchen Liu, and Xiang Chen. How convolutional neural networks see the world - A survey of convolutional neural network visualization methods. *Mathematical Foundations of Computing*, 1(2):149–180, 2018.
- [42] Danilo Jimenez Rezende, Shakir Mohamed, and Daan Wierstra. Stochastic backpropagation and approximate inference in deep generative models. In *Proceedings of the 31th International Conference on Machine Learning*, pages 1278–1286, 2014.
- [43] Marco Tulio Ribeiro, Sameer Singh, and Carlos Guestrin. “Why should I trust you?” Explaining the predictions of any classifier. In *Proceedings of the 22nd ACM SIGKDD International Conference on Knowledge Discovery and Data Mining*, pages 1135–1144, 2016.
- [44] Pouya Samangouei, Ardavan Saeedi, Liam Nakagawa, and Nathan Silberman. ExplainGAN: Model explanation via decision boundary crossing transformations. In *Proceedings of the 15th European Conference on Computer Vision*, pages 666–681, 2018.
- [45] Ramprasaath R. Selvaraju, Michael Cogswell, Abhishek Das, Ramakrishna Vedantam, Devi Parikh, and Dhruv Batra. Grad-CAM: Visual explanations from deep networks via gradient-based localization. In *Proceedings of the IEEE International Conference on Computer Vision*, pages 618–626, 2017.
- [46] Pavel Senin. Dynamic time warping algorithm review. 2008.
- [47] Sofia Serrano and Noah A. Smith. Is attention interpretable? In *Proceedings of the 57th Conference of the Association for Computational Linguistics*, pages 2931–2951, 2019.
- [48] Sumedha Singla, Brian Pollack, Junxiang Chen, and Kayhan Batmanghelich. Explanation by progressive exaggeration. In *Proceedings of the 8th International Conference on Learning Representations*, 2020.
- [49] Christian Szegedy, Wojciech Zaremba, Ilya Sutskever, Joan Bruna, Dumitru Erhan, Ian J. Goodfellow, and Rob Fergus. Intriguing properties of neural networks. In *Proceedings of the 2nd International Conference on Learning Representations*, 2014.
- [50] Cormen Thomas H., Leiserson Charles E., Rivest Ronald L., and Stein Clifford. *Introduction to Algorithms, Third Edition*. MIT Press, 2009.
- [51] Arnaud Van Looveren and Janis Klaise. Interpretable counterfactual explanations guided by prototypes. *arXiv preprint arXiv:1907.02584*, 2019.
- [52] Tianjun Xiao, Yichong Xu, Kuiyuan Yang, Jiaying Zhang, Yuxin Peng, and Zheng Zhang. The application of two-level attention models in deep convolutional neural network for fine-grained image classification. In *Proceedings of the IEEE Conference on Computer Vision and Pattern Recognition*, pages 842–850, 2015.
- [53] Jia-Wei Yan, Ci-Siang Lin, Fu-En Yang, Yu-Jhe Li, and Yu-Chiang Frank Wang. Semantics-guided representation learning with applications to visual synthesis. In *Proceedings of the 25th International Conference on Pattern Recognition*, pages 7181–7187, 2020.

- [54] Matthew D. Zeiler and Rob Fergus. Visualizing and understanding convolutional networks. In *Proceedings of the 13th European Conference on Computer Vision*, pages 818–833, 2014.
- [55] Zhilin Zheng and Li Sun. Disentangling latent space for VAE by label relevant/irrelevant dimensions. In *Proceedings of the IEEE/CVF Conference on Computer Vision and Pattern Recognition*, pages 12192–12201, 2019.
- [56] Bolei Zhou, Yiyou Sun, David Bau, and Antonio Torralba. Interpretable basis decomposition for visual explanation. In *Proceedings of the 15th European Conference on Computer Vision*, pages 119–134, 2018.
- [57] Xinqi Zhu, Chang Xu, and Dacheng Tao. Learning disentangled representations with latent variation predictability. In *Proceedings of the 16th European Conference on Computer Vision*, pages 684–700, 2020.

Supplementary Material

VAE-CE: Visual Contrastive Explanation using Disentangled VAEs

Yoeri Poels Vlado Menkovski
Eindhoven University of Technology, the Netherlands
{y.r.j.poels, v.menkovski}@tue.nl

1. Change Discriminator (CD)

The change discriminator (CD) is implemented as a binary classifier. It takes a pair of datapoints as input and predicts, in range $[0, 1]$, whether the change in datapoints is desirable, with 0 being undesirable and 1 being desirable. It is trained using pairs of datapoints depicting such changes, alongside a label indicating whether their change is desirable or not.

CD is heavily regularized in an attempt to deal with samples dissimilar to the training set (as it will classify interpolation pairs) and to exclude class-agnostic noise in its prediction. We use the disentangled VAE (from §3.1 in the main paper) as a base model for CD . In a separate pass we supply change pairs (x_a, x_b) and use their class-related embedding, z_{y_a} and z_{y_b} , to infer the change quality. We take the absolute difference of these embeddings and put them through a discriminative model to infer the final prediction for pair (x_a, x_b) :

$$CD(x_a, x_b) = DISC(|q_{\phi_y}(z_{y_a}|x_a) - q_{\phi_y}(z_{y_b}|x_b)|). \quad (1)$$

When training we minimize the binary cross-entropy between this prediction and change-quality labels y_{cd} . Simultaneously, we minimize the $ELBO$ for these samples, *i.e.* the first 3 terms of the loss in §3.1 of the main paper. The regular disentangled VAE objective is optimized in a separate pass, using regular datapoints and labels. An overview of the model is depicted in Fig. 1. During inference, *i.e.* while training VAE-CE, we only use the class-specific encoder and latent discriminator to make predictions. This submodel is depicted in Fig. 2.

2. Interpolation-graph complexity

To derive the size of the interpolation graph $\mathcal{G} = (V, E)$, we consider the graph as the discrete, dimension-wise interpolation of vector a to vector b , where $|a| = |b| = n$. Nodes denote intermediate states in this transition, and each edge corresponds to a (set of) dimension(s) being changed from a to b .

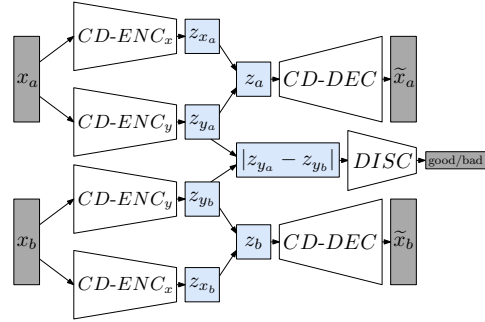


Figure 1: Components used during the change-discrimination pass of CD (*i.e.* the classifier components are omitted). The encoder and decoder distributions are written as $CD-ENC_y$, $CD-ENC_x$, and $CD-DEC$. We optimize the VAE objective and the change-discrimination objective. Note that the same encoder and decoder models are used for both datapoints.

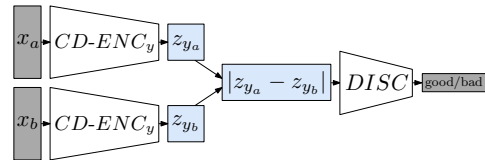


Figure 2: The components used when inferring a prediction from CD .

Each node in the graph considers one interpolation state, where for each dimension in this state, we pick the value from either a or b . As such, there are 2^n possible combinations, giving us $|V| = 2^n$.

To derive the total number of edges, we reason about the number of edges that are attached to each node. Each node has an outgoing edge towards all nodes that have changed dimension values from a_i to b_i , while not changing any such values from b_i back to a_i . As such, given a node with k dimensions already changed to b_i , we have $n - k$ dimensions that are yet to be changed. For each combination of $n - k$ changes we add an edge to the corresponding node,

giving $2^{n-k} - 1$ outgoing edges for a node with k already-changed values (we subtract one as we do not consider the case where none of these $n - k$ values are changed). The number of nodes that exist for each value of k is the number of combinations of size k given n values to change in total: $\binom{n}{k}$. The total number of edges can then be expressed by summing for all values of k . We denote and rewrite this sum as follows:

$$|E| = \sum_{k=0}^n \left[\binom{n}{k} (2^{n-k} - 1) \right] \quad (2)$$

$$= \sum_{k=0}^n \left[\binom{n}{k} (2^{n-k}) \right] - \sum_{k=0}^n \left[\binom{n}{k} \right] \quad (3)$$

$$= 3^n - 2^n, \quad (4)$$

using the Binomial Theorem[3] in step 4. As such, we get $|E| = 3^n - 2^n$.

3. Synthetic data generation

Synthetic datapoints are generated by using the class-shapes, as defined in §4.1 of the main paper, and adding noise. This process consists of two steps: (1) distorting the shape and (2) using this shape to create an image with varying stroke width.

Shape distortion. Shapes are distorted according to a randomly generated ‘vector field’ that determines how much each piece of the shape will move. This field is created using a normalizing force and 3 to 6 points that force the field to flow in a certain direction. These point forces are placed at random positions, have a random orientation and a random weight $\sim \mathcal{U}_{[3,6]}$. The direction of each point in the field is generated according to a weighted average of the forces. Each force’s weight, for a given position, is computed as $w_p = w_f \cdot \frac{1}{d(p,f)+1}$, where w_f is the force’s weight and $d(p, f)$ denotes the Euclidean distance between the position and the force.

The shape is distorted by computing the offset of the shape’s pieces according to this vector field, scaled according to an image-level weight $\sim \mathcal{U}_{[0.3,0.6]}$. In practice, each line consists of a subdivision of 20 evenly-spaced line segments, of which the start- and end-coordinates are transformed. The transformed shape is additionally rotated $\sim \mathcal{N}(0, \frac{\pi}{40})$ degrees. The new shape is centered and normalized to keep the size and position of the data constant. The entire distortion process is depicted in Fig. 3.

Stroke-width variation. Next, we generate the final datapoint using the distorted shape. Rather than applying a uniform line width, we vary the width throughout the image. This variation is produced by generating a ‘stroke-thickness field’ that determines the line width, as a proportion of the total image size, at any given point. This field is generated

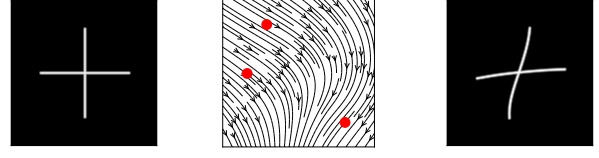


Figure 3: The distortion step of the data generation process.

similarly to the vector field. We sample a base stroke thickness $\sim \mathcal{U}_{[0.001,0.05]}$ and create 3 to 5 random points depicting a stroke-thickness force. Each of these points comes with a stroke thickness $\sim \mathcal{U}_{[0.001,0.05]}$, weight $\sim \mathcal{U}_{[3,6]}$, and decay exponent $\in \{2, 3, 4\}$. The stroke thickness at each point in the image is determined by a weighted average of the base thickness and the thickness of each force. Each force’s weight, for a given position, is computed as $w_p = w_f \cdot e^{-exp \cdot d(p,f)}$, where w_f depicts the weight parameter, exp the decay exponent, and $d(p, f)$ the Euclidean distance between the position and the force.

The final image is created by computing the distance of each pixel to its nearest line and checking with the stroke-field whether the pixel should be drawn as a line or not. On the edge of lines (in a constant range of 0.04) we linearly interpolate between white and black in order to create smooth edges. Following this process we can generate images of arbitrary resolution; an example of generating a 32x32 image is depicted in Fig. 4.

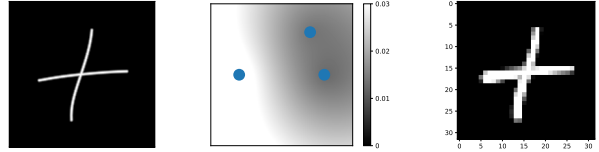


Figure 4: Creating the final datapoint by using a stroke-thickness field.

4. MNIST line-augmentation

MNIST datapoints are transformed into individual lines in order to be able to create change pairs. By hiding (sub)sets of individual lines we can create pairs differing in a single line. We consider a line to be a smooth curve, which we define as a sequence of points where the angle of the consecutive points (w.r.t. a horizontal line) does not change faster than some predefined limit. The process works in

three stages: (1) thinning images, (2) identifying starting points of lines and (3) generating lines.

Thinning images. To reduce an image to thin lines we follow the same procedure as [2]. This procedure considers first thresholding the image, *i.e.* marking all pixels above a specific value. The threshold is found by starting at 0 and increasing it iteratively until one of three conditions is reached: (1) the number of remaining (white) pixels drops under 50%, or (2) the number of 4-connected or 8-connected components changes, or (3) the threshold reaches 250 (given a pixel-range of $[0, 255]$). This (binary) image is thinned using the Zhang-Suen thinning algorithm[5]. An example of the thinning process is depicted in Fig. 5.

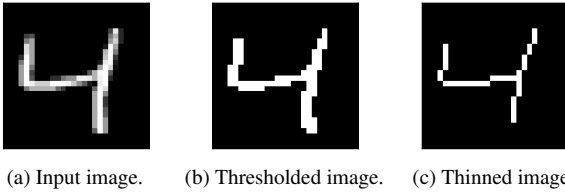


Figure 5: The thinning steps of augmenting MNIST-digits.

Identifying starting points. Lines are created by grouping neighboring white pixels together, where we consider 8-connected pixels as neighbors. To create lines from this representation, we first identify starting points and iteratively construct lines. We denote a starting pixel as a pixel with only one neighbor, where this neighboring pixel is connected to both the starting pixel and one other pixel. The first condition marks pixels likely to be the start point of a line, whereas the latter ensures that the starting pixel is not an ‘outlier’ pixel connected to a pixel in the middle of a line. If no such starting pixels can be found, the condition is relaxed to only the first condition. If still no starting pixels can be identified, we mark all pixels with the maximum number of neighbors as starting pixels (as these pixels likely lie on intersections of lines). The starting pixels for the example 4-image are depicted in Fig. 6.

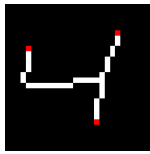


Figure 6: The starting pixels of the thinned image, marked as red pixels.

Line generation. Lines are identified by starting at an arbitrary starting pixel and iteratively adding pixels such that the overall line does not curve faster than a set limit ($\frac{\pi}{4}$, in our case). First, an arbitrary neighbor of the start-

ing pixel is added to the line. The angle between these two points (and a horizontal line) determines the line’s current angle. Then, points are iteratively added by checking the last-added point’s neighbors and adding the neighbor such that the angle of the line changes the least (ignoring already-added neighbors). The line angle is continuously updated according to the last 3 points added. When no neighboring points can be found such that the angle change does not exceed our chosen limit, the line is complete. The line-creation process is depicted in Fig. 7.

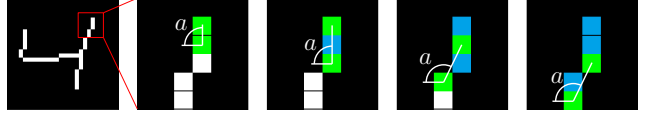
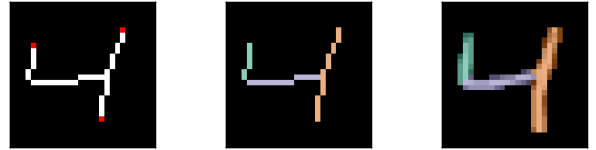


Figure 7: The line-creation process. We iteratively add neighbors such that angle a changes the least. Green pixels indicate the pixels currently determining the line angle, whereas blue pixels indicate the remaining pixels that were added to the line.

This process is repeated for all starting pixels. If we still have unmapped pixels, we create the remaining lines by starting from arbitrary points that neighbor already-found lines. Finally, outlier points (pixels with no neighbors) are added to their closest line. As the entire process can be noisy, it is possible that insignificant ‘lines’ were identified. As a post-processing step, we add these small lines (≤ 3 pixels) to their largest neighboring line (if a line is surrounded by only small lines, we add it to its neighbor-lines’ neighbor, and so on). To conclude, we create the line split of the source digit. Pixels of the (unmodified) datapoint are mapped to lines by assigning them to the closest line (the line with the minimal Euclidean distance between the to-be-mapped pixel and the closest pixel on the line). The result of this line-generation process is depicted in Fig. 8.



(a) The identified start- (b) The identified lines. (c) The final line split.
ing points.

Figure 8: The line-generation step of augmenting MNIST-digits, where each color indicates an identified line.

5. Model architecture

We first provide shared architectures, after which we provide method-specific architectures. All regular models use

8 latent dimensions per subspace, CD uses 16 latent dimensions per subspace. We denote (transposed) 2D convolutional layers as ‘ $(T)Conv2D(kernel\ size, stride, filters)$ ’ and use ‘SAME’ padding for all such layers. Fully connected layers are denoted as ‘ $FC(output\ size)$ ’. All models are implemented using Tensorflow[1].

5.1. Shared components

	Layer	Activation
x	Input ($32 \times 32 \times 1$)	
1	Conv2D($4 \times 4, 2, 32$)	LReLU(0.1)
2	Batch Normalization	
3	Conv2D($4 \times 4, 1, 64$)	LReLU(0.1)
4	Batch Normalization	
5	Conv2D($4 \times 4, 1, 128$)	LReLU(0.1)
6	Batch Normalization	
μ_y/μ_x	FC(8) from layer 6	
σ_y/σ_x	FC(8) from layer 6	

Table 1: The encoders, $q_{\phi_y}(z_y|x)$ and $q_{\phi_x}(z_x|x)$.

	Layer	Activation
z	Input (16)	
1	FC(32768)	LReLU(0.1)
2	Batch Normalization	
3	TConv2D($4 \times 4, 1, 64$)	LReLU(0.1)
4	Batch Normalization	
5	TConv2D($4 \times 4, 1, 32$)	LReLU(0.1)
6	Batch Normalization	
\tilde{x}	TConv2D($4 \times 4, 2, 1$)	Sigmoid

Table 2: The decoder, $p_{\theta}(x|z_y, z_x)$.

	Layer	Activation
z_y	Input (8)	
\tilde{y}	FC(10)	Softmax

Table 3: The label classifier, $q_{\psi_y}(y|z_y)$.

	Layer	Activation
z_x	Input (8)	
1	FC(50)	LReLU(0.1)
2	Batch Normalization	
\tilde{y}	FC(10)	Softmax

Table 4: The adverse label classifier, $q_{\psi_x}(y|z_x)$.

5.2. LVAE

	Layer	Activation
z_{y_i}	Input (1)	
\tilde{d}_i	FC(2)	Softmax

Table 5: The dimension-label classifiers.

	Layer	Activation
$z_{y_{ic}}$	Input (7)	
1	FC(50)	LReLU(0.1)
2	Batch Normalization	
\tilde{d}_i	FC(2)	Softmax

Table 6: The complementary dimension-label classifiers.

5.3. VAE-CE

	Layer	Activation
x	Input ($32 \times 32 \times 1$)	
1	Conv2D($4 \times 4, 2, 32$)	LReLU(0.1)
2	Batch Normalization	
3	Dropout(0.3)	
4	Conv2D($4 \times 4, 1, 64$)	LReLU(0.1)
5	Batch Normalization	
6	Dropout(0.3)	
7	Conv2D($4 \times 4, 1, 128$)	LReLU(0.1)
8	Batch Normalization	
9	Dropout(0.3)	
$real$	FC(2)	Softmax

Table 7: The realism discriminator, D .

5.4. CD

	Layer	Activation
x	Input ($32 \times 32 \times 1$)	
1	Conv2D($4 \times 4, 2, 32$)	LReLU(0.1)
2	Batch Normalization	
3	Conv2D($4 \times 4, 1, 128$)	LReLU(0.1)
4	Batch Normalization	
μ_y/μ_x	FC(16) from layer 4	
σ_y/σ_x	FC(16) from layer 4	

Table 8: CD ’s encoders.

	Layer	Activation
z	Input (32)	
1	FC(32768)	LReLU(0.1)
2	Batch Normalization	
3	TConv2D($4 \times 4, 1, 32$)	LReLU(0.1)
4	Batch Normalization	
\tilde{x}	TConv2D($4 \times 4, 2, 1$)	Sigmoid

Table 9: CD ’s decoder.

	Layer	Activation
z_y or z_x	Input (16)	
1	FC(50)	LReLU(0.1)
2	Batch Normalization	
\tilde{y}	FC(10)	Softmax

Table 10: CD ’s label-disentanglement classifiers.

	Layer	Activation
$ z_{y_a} - z_{y_b} $	Input (16)	
1	FC(50)	LReLU(0.1)
2	Batch Normalization	
3	Dropout(0.3)	
$change$	FC(2)	Softmax

Table 11: The latent-change discriminator, $DISC$.

6. Hyperparameters and training

6.1. Loss functions

First, we briefly restate the loss functions. All methods extend DVAE: We sum the DVAE loss and the method-specific loss. Note that CD also extends DVAE.

DVAE’s loss denotes the class-disentangled VAE optimization, as described in §3.1 of the main paper:

$$\mathcal{L}_{\theta, \phi_y, \phi_x, \psi_y}(x, y) = \beta_y KL(q_{\phi_y}(z_y|x)||p_{\theta}(z)) \quad (5)$$

$$+ \beta_x KL(q_{\phi_x}(z_x|x)||p_{\theta}(z)) \quad (6)$$

$$- \mathbb{E}_{q_{\phi_y}(z_y|x), q_{\phi_x}(z_x|x)} [\log p_{\theta}(x|z_y, z_x)] \quad (7)$$

$$- \alpha \mathbb{E}_{q_{\phi_y}(z_y|x)} [\log(q_{\psi_y}(y|z_y))] \quad (8)$$

$$+ \alpha \mathbb{E}_{q_{\phi_x}(z_x|x)} [\log(q_{\psi_x}(y|z_x))], \quad (9)$$

$$\mathcal{L}_{\psi_x}(x, y) = -\mathbb{E}_{q_{\phi_x}(z_x|x)} [\log(q_{\psi_x}(y|z_x))], \quad (10)$$

LVAE’s loss optimizes individual dimensions using auxiliary classifiers. We denote dimension labels as d_i , individual dimensions as z_{y_i} , and the complementary dimensions (all dimensions but i) as $z_{y_{ci}}$. We use a classifier for each

label i , denoted as categorical distribution $q_{\psi_{di}}(d_i|z_{y_i})$, and an adversarial classifier for the complementing dimensions ci , denoted as categorical distribution $q_{\psi_{dci}}(d_i|z_{y_{ci}})$. n_c denotes the number of concepts. The extra loss terms can be denoted as follows:

$$\mathcal{L}_{\theta, \phi_y, \psi_{di}}(x, y, d_i) = -\alpha_d \log(q_{\psi_{di}}(d_i|z_{y_i})) \quad (11)$$

$$+ \alpha_d \log(q_{\psi_{dci}}(d_i|z_{y_{ci}})), \quad (12)$$

$$\mathcal{L}_{\psi_{dci}}(x, y, d_i) = -\log(q_{\psi_{dci}}(d_i|z_{y_{ci}})), \quad (13)$$

$$\mathcal{L}_{LVAE}(x, y, d) = \sum_i^{n_c} (\mathcal{L}_{\theta, \phi_y, \psi_{di}}(x, y, d_i) \quad (14)$$

$$+ \mathcal{L}_{\psi_{dci}}(x, y, d_i)). \quad (15)$$

VAE-CE’s loss considers the pair-based dimension conditioning procedure as described in §3.2 of the main paper. We create samples \tilde{x}_{p_a} and \tilde{x}_{p_b} (from datapoints that are used in the DVAE objective) and optimize the main VAE using CD and D . Additionally, we train D to distinguish between real/fake datapoints as a binary classification task, using datapoint-label pairs (x, y_d) . We either use the synthesized datapoints and a 0-label, or training datapoints and a 1-label. The loss can be denoted as follows:

$$\mathcal{L}_{\theta, \phi_y, \phi_x}(\tilde{x}_{p_a}, \tilde{x}_{p_b}) = -\alpha_r \log(D(\tilde{x}_{p_a})) \quad (16)$$

$$- \alpha_r \log(D(\tilde{x}_{p_b})) \quad (17)$$

$$+ \alpha_p n_y \frac{|z_{p_a} - z_{p_b}|}{|z_{y_a} - z_{y_b}|} \cdot \log(CD(\tilde{x}_{p_a}, \tilde{x}_{p_b})), \quad (18)$$

$$\mathcal{L}_D(x, y_d) = -\log(D(y_d|x)). \quad (19)$$

GVAE and ADA-GVAE are optimized using the $ELBO$, i.e. equations (5), (6), and (7). We use specific pairings of datapoints and average out dimensions. Since these datapoints might not have class labels, we compute their loss w.r.t. the $ELBO$ in a separate pass.

CD’s loss optimizes the change-discrimination objective. We denote the change-quality label as y_{cd} , and infer a change-quality prediction of a pair (x_a, x_b) . The resulting loss can be denoted as follows:

$$CD(x_a, x_b) = DISC(|q_{\phi_y}(z_{y_a}|x_a) - q_{\phi_y}(z_{y_b}|x_b)|), \quad (20)$$

$$\mathcal{L}_{\phi_y, DISC}(x_a, x_b, y_{cd}) = -\alpha_c \log(CD(y_{cd}|x_a, x_b)). \quad (21)$$

Finally, we note that for models using multiple training passes with uneven numbers of datapoints (GVAE, ADA-GVAE, and CD), we scale the respective losses by this ratio in order to balance the different passes.

6.2. Hyperparameter optimization

The settings shared between all training procedures are depicted in Table 12. We tune the hyperparameters as follows. First, we identify a non-degenerate solution by hand,

defined as a solution where none of the objectives are ignored (*i.e.* no collapsed latent spaces, uninformative classifiers, or all-zero outputs). Next, we define a range of parameters around this solution, and explore all configurations in this range. The hyperparameters are provided in Table 13, whereas their explored values are denoted in Table 14.

We use the *eac* for model selection, using 90 (a, b) pairs (note that these pairs are distinct from the pairs used for the final results). We generate interpolations using all methods (*sm*, *dim*, and *graph* for VAE-CE) and take minimum *eac* out of these. As computing the *eac* requires access to the ground-truth generating process, we search for hyperparameters using the synthetic data. The identified parameters are also used for the MNIST models.

Each model is trained for $\approx 2\,000\,000$ steps: 20 epochs on the synthetic dataset and 33 epochs on MNIST. We found that training models with fewer steps generally resulted in worse *eac*-values, whereas training for significantly longer did not improve (and sometimes regressed) the *eac*-score.

For each model type we consider the Cartesian product of the hyperparameter values denoted in Table 14. We train each configuration four times, giving us a total of 176 models. For each configuration we compute the average *eac* and select the hyperparameters corresponding to the lowest cost. These identified hyperparameters are depicted in Table 15. An overview of all model runs is provided in Fig. 9.

CD is trained beforehand. For simplicity, we used a single configuration that gave a satisfactory test-set change-pair accuracy (96.4% on the synthetic data and 87.1% on MNIST-pairs). This configuration is depicted in Table 16. *CD* was trained for 5 000 000 steps (for both datasets).

Setting	Value
Batch size	128
Optimizer	Adam[4]
Adam: learning rate	0.001
Adam: β_1	0.9
Adam: β_2	0.999
Adam: ϵ	0.0001

Table 12: Shared settings.

Meaning	Model
β_y z_y KL divergence weight	<i>all</i>
β_x z_x KL divergence weight	<i>all</i>
α class-label classification weight	<i>all</i>
α_d per-dimension classification weight	LVAE
α_r <i>D</i> -prediction weight	VAE-CE
α_p <i>CD</i> -prediction weight	VAE-CE

Table 13: All hyperparameters.

Model	Values
DVAE	β_y {2, 4} α {5, 10, 15}
LVAE	β_y {1, 2} α {5, 7} α_d {20, 25, 30}
GVAE	β_y {1, 2, 4} α {2, 4, 6}
ADA-GVAE	β_y {1, 2, 4} α {1, 2, 4}
VAE-CE	β_y {2, 4} α {5, 7} α_p {3, 5}

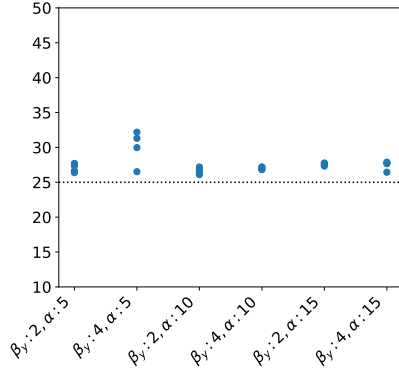
Table 14: All explored hyperparameter values. Parameters not mentioned are set to 1. The Cartesian product of the per-parameter values denotes all configurations we train.

Model	Value
DVAE	β_y 2 α 10
LVAE	β_y 1 α 7 α_d 20
GVAE	β_y 1 α 6
ADA-GVAE	β_y 1 α 4
VAE-CE	β_y 2 α 7 α_p 3

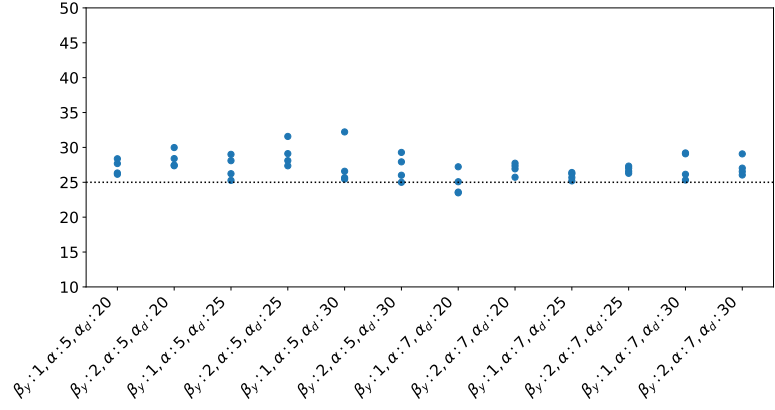
Table 15: The selected hyperparameter values.

Meaning	Value
β_y z_y KL divergence weight	1
β_x z_x KL divergence weight	0.5
α class-label classification weight	16
α_c <i>DISC</i> classification weight	50

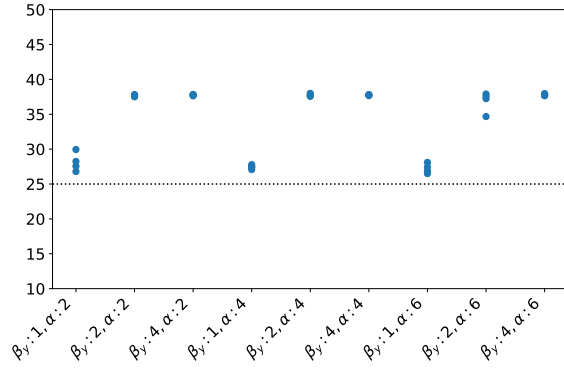
Table 16: *CD* hyperparameters.



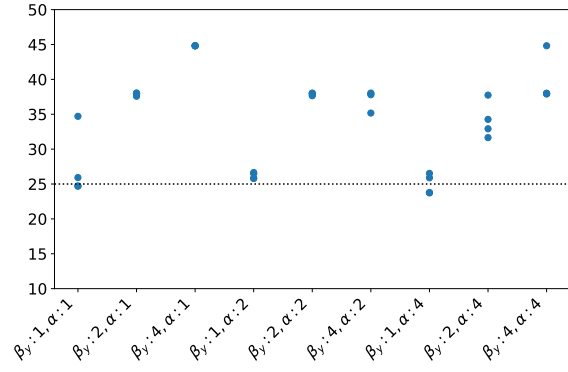
(a) DVAE



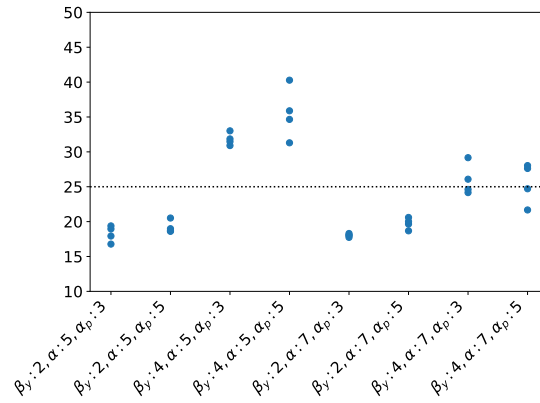
(b) LVAE



(c) GVAE



(d) ADA-GVAE



(e) VAE-CE

Figure 9: The minimum *eac* of each model-run (on validation data). The x-axis depicts the different configurations, whereas the y-axis depicts the *eac* (lower is better).

References

- [1] Martín Abadi, Ashish Agarwal, Paul Barham, Eugene Brevdo, Zhifeng Chen, Craig Citro, Greg S. Corrado, Andy Davis, Jeffrey Dean, Matthieu Devin, Sanjay Ghemawat, Ian Goodfellow, Andrew Harp, Geoffrey Irving, Michael Isard, Yangqing Jia, Rafal Jozefowicz, Lukasz Kaiser, Manjunath Kudlur, Josh Levenberg, Dandelion Mané, Rajat Monga, Sherry Moore, Derek Murray, Chris Olah, Mike Schuster, Jonathon Shlens, Benoit Steiner, Ilya Sutskever, Kunal Talwar, Paul Tucker, Vincent Vanhoucke, Vijay Vasudevan, Fernanda Viégas, Oriol Vinyals, Pete Warden, Martin Wattenberg, Martin Wicke, Yuan Yu, and Xiaoqiang Zheng. TensorFlow: Large-scale machine learning on heterogeneous systems, 2015. Software available from tensorflow.org.
- [2] Edwin D de Jong. Incremental sequence learning. *arXiv preprint arXiv:1611.03068*, 2016.
- [3] Ronald L. Graham, Donald E. Knuth, Oren Patashnik, and Stanley Liu. Concrete mathematics: a foundation for computer science. *Computers in Physics*, 3(5):106–107, 1989.
- [4] Diederik P. Kingma and Jimmy Ba. Adam: A method for stochastic optimization. In *Proceedings of the 3rd International Conference on Learning Representations*, 2015.
- [5] T. Y. Zhang and Ching Y. Suen. A fast parallel algorithm for thinning digital patterns. *Communications of the ACM*, 27(3):236–239, 1984.